land

MDPI

Article

A Physics-Informed Empirical Model for Predicting Vegetation-Related InSAR Coherence

Chengxian Ma, Songping Li, Xiaowen Wang and Guoxiang Liu *

Faculty of Geosciences and Engineering, Southwest Jiaotong University, Chengdu 611756, China; 2024211904@my.swjtu.edu.cn (C.M.); hjyiiii@my.swjtu.edu.cn (S.L.); insarwxw@swjtu.edu.cn (X.W.)
* Correspondence: rsgxliu@swjtu.edu.cn

Abstract

Vegetation-induced temporal decorrelation limits the reliability of time-series InSAR measurements over densely vegetated areas. Existing empirical models generally use NDVI from a single acquisition and therefore cannot represent vegetation changes between the two SAR acquisitions. This study investigates coherence prediction for interferometric pairs with an approximately 60-day temporal baseline. Guided by the physical understanding of vegetation-related decorrelation, we use two complementary predictors: the sum of the NDVI values from the two acquisition dates, representing overall vegetation cover, and their absolute difference, representing inter-acquisition vegetation change. Separate exponential response functions are fitted and combined through a weighted additive formulation to construct a physically motivated dual-NDVI empirical coherence model (PICM). The additive formulation is an empirical predictive representation rather than a direct derivation from the multiplicative decomposition of coherence. The model is calibrated using correlation-screened samples from the Juye area, after which its coefficients are held fixed and applied to all valid pixels without correlation-based preselection. Independent spatial validation is conducted in the Gu'an area without recalibration. The proposed model achieves an error standard deviation of 0.166 and a mean error of −0.048 in Gu'an, compared with 0.190 and 0.089 for the single-NDVI model, respectively. The results demonstrate that incorporating both vegetation cover and inter-acquisition vegetation change improves coherence prediction for the approximately 60-day interferometric pairs examined. Its applicability to shorter temporal baselines and other land-cover conditions requires further investigation.

Keywords: InSAR; SAR Coherence; Interferometric SAR image pair; NDVI

Check for updates

Academic Editor: Eusebio Cano Carmona

Received: 18 September 2026
Revised: 8 October 2026
Accepted: 13 October 2026
Published: 17 October 2026

Copyright: © 2026 by the authors. Licensee MDPI, Basel, Switzerland. This article is an open access article distributed under the terms and conditions of the Creative Commons Attribution (CC BY) license.

1. Introduction

Interferometric Synthetic Aperture Radar (InSAR) has been proven to be an effective tool for monitoring surface deformation, offering advantages such as all weather, day and night, and large-scale monitoring capability [1–7]. However, as a technique based on repeated observations, InSAR still faces a series of challenges in practical applications. Among them, temporal decorrelation is one of the key factors that reduces phase stability in interferograms, thereby affecting the accuracy of deformation monitoring [8]. The phase discrepancies in radar echo signals brought on by variations in surface scattering properties over time are the physical basis of temporal decorrelation. To quantitatively assess and mitigate the effects of temporal decorrelation, coherence is widely used as a key indicator for evaluating InSAR data quality and measurement reliability. Coherence can typically be

divided into two components: spatial coherence and temporal coherence. Among them, spatial coherence can be calculated using theoretical models. Temporal coherence, however, cannot be measured directly. Instead, it is typically isolated by removing other coherence components based on the principle of coherence composition [9].

Temporal decorrelation mainly arises from changes in surface scattering characteristics between satellite acquisitions [10–12]. In vegetated areas, changes in vegetation conditions can constitute an important source of interferometric coherence loss because vegetation growth, senescence, and disturbance may alter the dielectric properties, spatial configuration, and stability of scatterers within a resolution cell. However, the observed interferometric coherence is an integrated response to multiple decorrelation mechanisms, and vegetation-related changes may affect temporal stability, volume scattering, and canopy structure simultaneously. Therefore, establishing a quantitative relationship between vegetation conditions and observed interferometric coherence provides a practical approach for assessing InSAR data quality, without necessarily isolating individual physical decorrelation components. Several studies have investigated this relationship. Although coherence has been widely used for land-cover classification, the quantitative relationship between coherence and vegetation coverage has not yet been fully established [13]. Vegetation height and density are both important factors affecting interferometric coherence [14]. In general, coherence tends to decrease with increasing vegetation density [15]. Other studies have also reported nonlinear relationships between coherence and vegetation indices, although the stability and transferability of these relationships require further investigation [16]. Most existing studies have focused on qualitative or region-specific relationships, and a generally applicable quantitative relationship between vegetation conditions and interferometric coherence remains to be established.

The Normalized Difference Vegetation Index (NDVI) is widely used to characterize vegetation greenness and coverage and can be derived from freely available optical satellite imagery, such as Landsat data. Previous studies have demonstrated empirical relationships between NDVI and observed interferometric coherence [17–22], providing a basis for using NDVI as an observable predictor of vegetation-related variations in SAR coherence. Bai et al. established an empirical relationship between interferometric coherence and NDVI and found that periods with relatively low NDVI values were generally more suitable for deformation monitoring [18]. Liu et al. investigated the relationship between coherence and NDVI in southern China using linear and power-function models. They identified a negative relationship between the two variables, with the power-function model achieving better prediction accuracy than the linear model. Chen et al. developed a three-stage coherence estimation model based on Landsat-derived NDVI [23]. These studies provide both theoretical and empirical support for using NDVI to predict interferometric coherence. However, most existing models use NDVI from only one acquisition date and therefore cannot explicitly describe changes in vegetation conditions between the two SAR acquisitions forming an interferometric pair. This limitation may reduce their predictive performance across different months or seasons, particularly during periods of rapid vegetation change.

Existing studies on the vegetation–coherence relationship can be broadly divided into two groups, each with a distinct limitation. Empirical coherence–NDVI models are operationally attractive because NDVI is readily available, but most of them use NDVI from only one acquisition date and therefore cannot describe the change in vegetation conditions between the two SAR acquisitions forming an interferogram. Physical decorrelation models provide a more mechanistic description but generally require parameters such as vegetation height, canopy structure, and motion variance, which are difficult to retrieve operationally [24].

This study bridges these two approaches by using two readily observable quantities: the sum and the absolute difference of the NDVI values corresponding to the reference and secondary SAR acquisitions. The NDVI sum is used to characterize the overall vegetation condition of the interferometric pair, whereas the absolute NDVI difference is used to characterize the magnitude of inter-acquisition vegetation change. Changes in vegetation conditions may contribute to temporal decorrelation by altering scattering properties between acquisitions, but they may also be associated with changes in volume scattering, canopy structure, and other surface properties. Therefore, the two NDVI-derived variables are treated as complementary empirical predictors of observed interferometric coherence rather than as direct or exclusive measurements of individual physical decorrelation components.

Guided by the physical understanding that interferometric coherence is jointly affected by multiple decorrelation mechanisms, separate empirical response functions are fitted for the two NDVI-derived predictors and combined to predict the observed overall coherence. The resulting formulation is therefore a physically motivated dual-NDVI empirical coherence model rather than a direct derivation or inversion of the multiplicative coherence decomposition.

The main contributions of this study are: (1) the physically motivated selection of two complementary NDVI predictors that characterize the overall vegetation condition and inter-acquisition vegetation change, respectively, without assigning either predictor to a unique physical decorrelation component; (2) a controlled Monte Carlo experiment evaluating the predictive advantage of the proposed PICM over the conventional single-NDVI model; and (3) validation using Sentinel-1 data from two regions of the North China Plain, with the Juye area in Shandong Province used for model calibration and the Gu'an area in Hebei Province used for independent spatial validation, together with a practical application to prior coherence estimation for time-series InSAR in densely vegetated regions.

2. Materials and Methods

2.1. Study Area

This study selects a test area with dense vegetation cover, located in the northeastern part of Heze City, Shandong Province, China. The area mainly includes Yuncheng County, Juye County, and Jiaxiang County, covering approximately 1000 square kilometers. Situated at the southern edge of the North China Plain, the region has a temperate monsoon climate with distinct seasons and moderate precipitation, making it suitable for agricultural production. The terrain is flat, with elevations ranging between 30 and 50 m. The land surface is primarily covered by contiguous farmland, mainly growing dryland crops such as winter wheat and summer corn, supplemented by a small number of greenhouses and orchards. Influenced by the monsoon climate, vegetation coverage in the farmland exhibits pronounced seasonal variations. During the growing season (May to October), vegetation coverage exceeds 90%, whereas during the winter fallow period (November to April of the following year), more than 60% of the land surface remains bare. In addition, this area is affected by deformation associated with the Juye mining area [8].

The validation area is located along the railway line near Beijing Daxing International Airport, centered around Gu'an County, Langfang City, Hebei Province. It includes towns under its jurisdiction, such as Gu'an Town, Gongcun Town, and Dongwan Township, covering an area of approximately 1000 square kilometers. This region lies within the alluvial zone of the North China Plain and features flat terrain. Land surface cover consists primarily of farmland, forestland, and rural settlements, with seasonal fluctuations in vegetation coverage being significant. New transportation networks, such as the Jingde Expressway and the Airport North Line Expressway, have been constructed in the area,

leading to a high risk of surface disturbances caused by engineering activities. This region provides representative samples of high dynamic land surface conditions for validating the InSAR deformation monitoring method that integrates NDVI. The locations of the study area and validation area are shown in Figure 1.

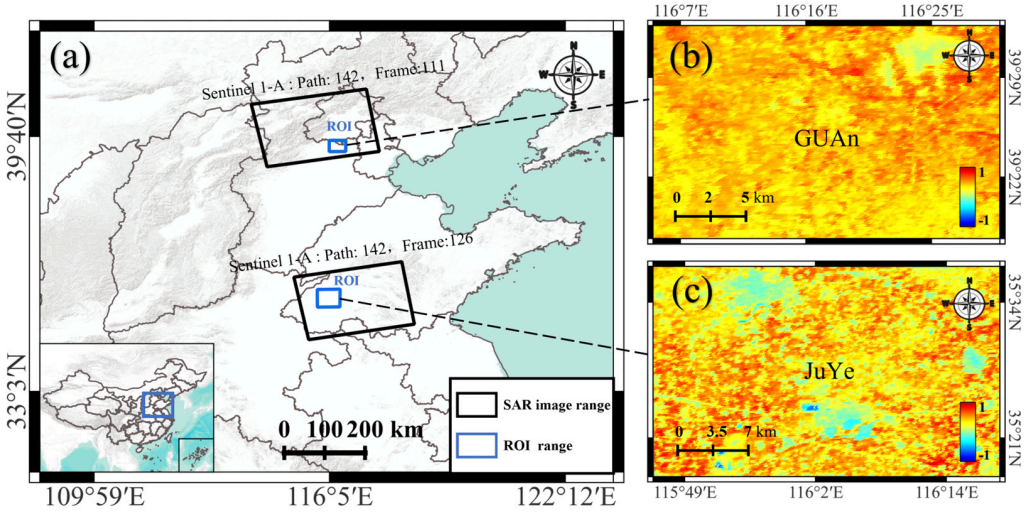


Figure 1. The locations of the test area and validation area (**a**). The NDVI maps for the test area (**b**) and validation area (**c**).

2.2. Data

The experimental data collected in this study primarily include .Sentinel-1A SAR data from the European Space Agency (ESA, Paris, France) and Landsat optical imagery(United States Geological Survey, Reston, VA, USA) (with a 16-day revisit cycle) used to derive the NDVI values. Sentinel-1A SAR data from the two study areas were processed using GAMMA software (version 2020, GAMMA Remote Sensing AG, Gümligen, Switzerland) to validate the proposed method. The Sentinel-1A satellite was launched by ESA in April 2014, with a carrier wavelength of 5.54 cm (C-band) [25]. Its spatial and temporal resolution, as well as its swath coverage, have been significantly improved compared to previous satellites (ERS/Envisat), with a revisit cycle shortened to 12 days.

The SAR data consist of 10 images acquired in the Juye area from February 2018 to December 2018, and 10 images acquired in the Gu'an area from February 2019 to December 2019. To perform topographic phase compensation and geocoding, 30 m resolution SRTM data (National Aeronautics and Space Administration, Washington, DC, USA) were used as an external reference DEM [26]. POD precision orbit data released by the European Space Agency were also used to correct orbital errors. To match each SAR scene with its corresponding NDVI, interpolation was performed to obtain NDVI values for each SAR acquisition date. Because Landsat observations were not always available on the exact SAR acquisition dates, NDVI at each SAR acquisition date was estimated by linear interpolation between the temporally adjacent valid Landsat NDVI observations.

In this study, interferometric pairs with a temporal baseline of approximately 60 days were selected to construct the dataset. Previous studies have shown that conventional single-date NDVI models can effectively characterize interferometric coherence for relatively short or moderate temporal baselines [27–29]. Under shorter-baseline conditions, vegetation changes between acquisitions are generally limited and interferometric coherence is relatively well preserved. Consequently, the additional benefit of introducing an inter-acquisition vegetation-change predictor is expected to be limited. This specific interval was determined based on two primary considerations. First, as illustrated in Figure 2, a study-specific and practical temporal interval is long enough to capture signifi-

cant temporal decorrelation driven by vegetation dynamics, yet short enough to preserve a reliable level of overall coherence for analysis. Statistical evaluation reveals that 90% of the high coherence pairs (coherence > 0.8) in the study area fall within this temporal window. Conversely, substantially longer baselines may lead to widespread decorrelation, whereas shorter baselines generally exhibit limited vegetation change and relatively high coherence, reducing the practical need for an additional inter-acquisition vegetation-change predictor. Second, configuring the temporal baseline to 60 days facilitates the temporal alignment of multi-source datasets. Given that the regular revisit cycles of Sentinel-1A SAR and the Landsat 8 optical satellite are 12 days and 16 days, respectively, a 60-day interval serves as a highly practical temporal window. This temporal baseline effectively facilitates the tight chronological pairing of master slave SAR images with their temporally closest Landsat NDVI acquisitions.

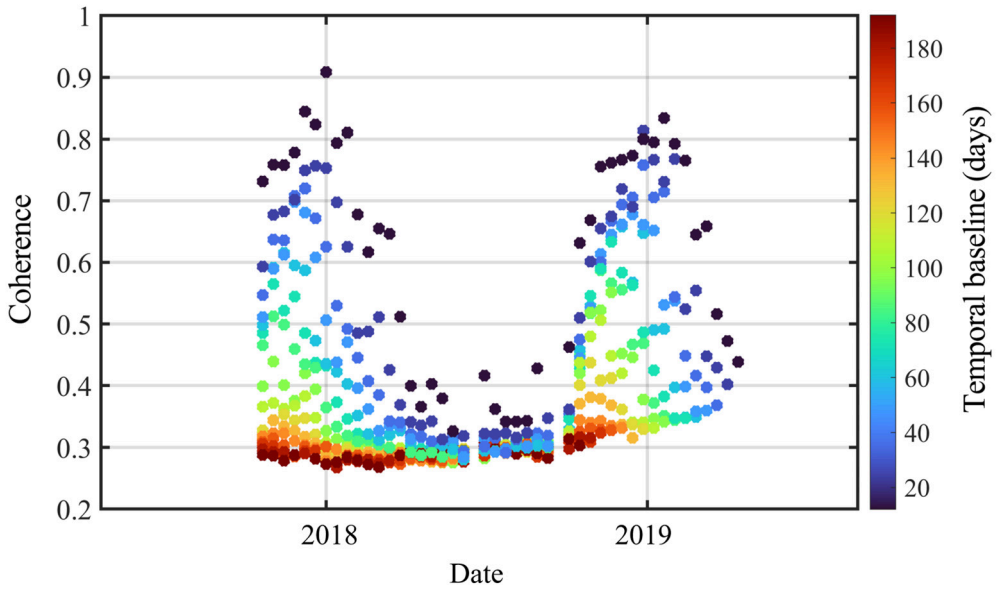


Figure 2. Seasonal variations of interferometric coherence and the impact of temporal baselines in the study area.

3. Physics Informed Empirical Coherence Model

This section presents the development of a physics-informed empirical coherence model that incorporates vegetation conditions at both SAR acquisition dates. The sum and absolute difference of the reference and secondary NDVI values are used as complementary predictors to represent vegetation cover and its change between acquisitions. Model development comprises three stages. First, spatially coregistered NDVI and interferometric coherence observations are screened using a local correlation criterion to construct calibration samples (Section 3.1). Second, the relationships between the two NDVI predictors and coherence are examined and, together with physical considerations of decorrelation, used to formulate the joint model and a single-NDVI benchmark (Section 3.2). Third, the model parameters are estimated from the calibration samples to obtain the fitted models used in the subsequent experiments (Section 3.3). This workflow connects sample selection, model formulation, and parameter estimation within a common framework for coherence prediction. Figure 3 summarizes the workflow of the proposed method.

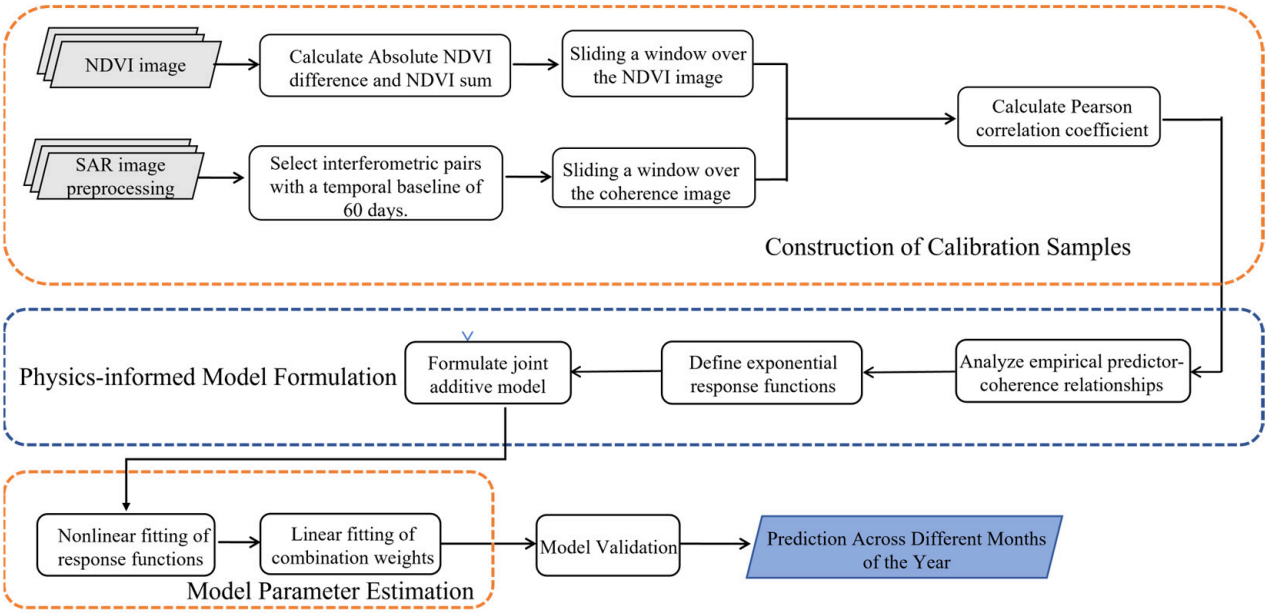


Figure 3. Workflow of the proposed coherence modeling method.

3.1. Construction of Calibration Samples

Calibration samples are constructed to support the empirical relationship analysis in Section 3.2 and the parameter estimation in Section 3.3. Following the local correlation-based sampling approach of Chen et al. [28], observations are selected according to the local association between the NDVI-derived predictors and interferometric coherence. The purpose of this screening is to identify vegetation-sensitive observations suitable for calibrating the vegetation-related coherence model, rather than to construct a sample set representative of all landscape conditions. Weak local correlation is not treated as evidence of measurement error, but may indicate that vegetation is not the dominant factor controlling coherence within the corresponding window. It should be emphasized that correlation-based screening is used only for calibration-sample construction; after parameter estimation, the fitted model is applied to all valid pixels without correlation-based preselection.

For each interferometric pair, NDVI observations are temporally matched to the reference and secondary SAR acquisition dates and spatially coregistered with the coherence image. Two predictors are then constructed at each pixel i:

$$S\_ndvi_i = NDVI_{m,i} + NDVI_{s,i}, \quad D\_ndvi_i = |NDVI_{m,i} - NDVI_{s,i}| \tag{1}$$

Here, m and s denote the reference and secondary acquisitions, respectively. Each observation comprises the NDVI sum S_ndvi, the absolute NDVI difference D_ndvi, and the observed interferometric coherence γ_i. These paired predictors represent vegetation cover and inter acquisition change, respectively; their roles in the model formulation are discussed in Section 3.2.

Sampling is performed using spatially corresponding 6 × 6 moving windows. At each window position, the Pearson correlation coefficient is calculated separately between coherence and each predictor. For a predictor X, where X denotes either S_ndvi or D_ndvi, the local coefficient is

$$r_X = \frac{\sum_{k=1}^{N} (X_k - \overline{X})(\gamma_k - \overline{\gamma})}{\sqrt{\sum_{k=1}^{N} (X_k - \overline{X})^2 \sum_{k=1}^{N} (\gamma_k - \overline{\gamma})^2}} \quad (2)$$

where N is the number of paired observations used within the window, and $\overline{X}$ and $\overline{\gamma}$ are their respective window means. The screening threshold has a correlation magnitude of 0.8. Pixels in windows satisfying the correlation criterion are retained as calibration candidates for the corresponding predictor, and the procedure is repeated across the image. To ensure a methodologically consistent comparison, the single-NDVI benchmark is constructed using the same moving-window size, correlation-threshold magnitude, and data-quality criteria. Thus, the proposed model and the single-NDVI benchmark are compared within the same correlation-based calibration framework, although the predictors may retain different sets of calibration pixels. The sampling procedure is illustrated in Figure 4.

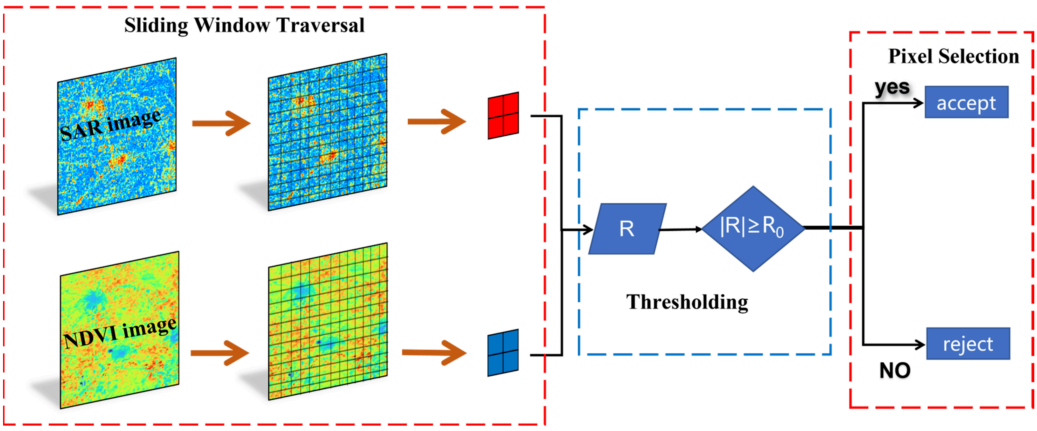


Figure 4. Local correlation-based sampling procedure. R is the local Pearson correlation coefficient and R_0 denotes the screening threshold.

Table 1 summarizes the retained pixel counts for the interferometric pairs considered. These counts describe sample availability under the different screening criteria; a larger retained sample count does not by itself establish a stronger overall relationship or better predictive performance.

Table 1. Number of pixels retained under each correlation-based screening criterion.

Predictor	8 February–9 April 2018	9 April–8 June 2018	8 June–7 August 2018	7 August–6 October 2018	6 October–5 December 2018
Single NDVI	8460	716	2992	6488	756
NDVI sum	13,320	5760	4364	4572	3890
NDVI difference	2844	5184	2742	6806	1370

The June–August interferometric pair in the Juye area supplies the correlation-screened calibration observations used to examine the predictor–coherence relationships in Section 3.2 and to estimate the model parameters in Section 3.3. After parameter estimation, all fitted coefficients are held fixed. The calibrated models are first applied to all valid pixels over the complete Juye area, including pixels not retained during calibration, and are subsequently transferred directly to the independent Gu'an validation area without recalibration. Therefore, correlation-based screening is used only for parameter estimation, whereas full-area prediction and validation are performed without correlation-based pixel preselection.

3.2. Physics Informed Model Formulation

The model relates the paired vegetation predictors defined in Equation (1) to observed interferometric coherence. Physical considerations motivate the choice of predictors, while their response functions and combination are specified empirically. When decorrelation mechanisms can be treated as statistically independent, the observed coherence can be approximated by a product of contributions. Equation (3) is introduced to provide the physical background for identifying the vegetation-related factors affecting coherence. It is not used here to derive the algebraic form of the subsequent empirical model.

$$\gamma \approx \gamma_{SNR} \cdot \gamma_{spatial} \cdot \gamma_{vol} \cdot \gamma_{temporal} \tag{3}$$

Here, γ_{SNR} represents the contribution associated with thermal noise, $\gamma_{spatial}$ describes geometric decorrelation, γ_{vol} represents volume decorrelation, and $\gamma_{temporal}$ describes changes in scattering properties between acquisitions. The NDVI sum *S_ndvi* is used as a proxy for vegetation cover at the two acquisition dates, whereas the absolute NDVI difference *D_ndvi* represents the magnitude of change in vegetation greenness. These optical predictors do not directly measure the individual coherence components, and their use does not imply that S_ndvi and *D_ndvi* are statistically independent.

The calibration samples described in Section 3.1 are used to examine the empirical relationships between each predictor and coherence. Figure 5 shows decreasing coherence with increasing *S_ndvi* and with increasing *D_ndvi* in the selected samples. The fitted curve in Figure 5b decreases and becomes flatter at larger NDVI differences. These patterns motivate the use of decreasing response functions, although the separately screened relationships do not establish the independent contribution of either predictor.

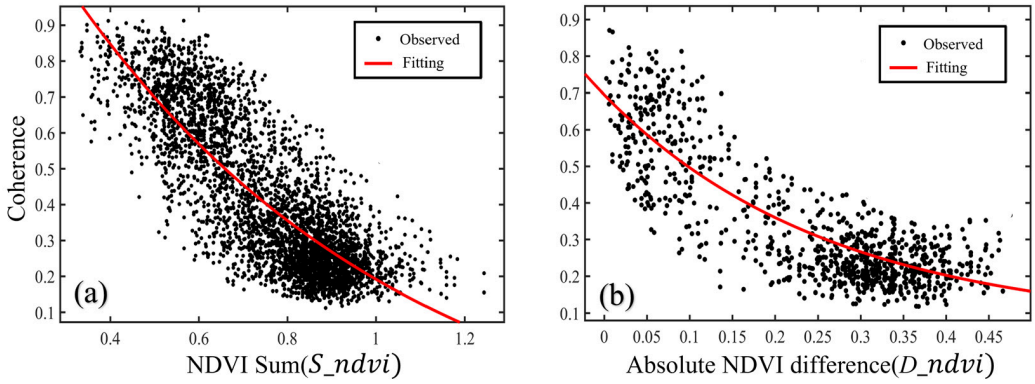


Figure 5. Relationships between observed coherence and (**a**) the NDVI sum S_ndvi and (**b**) the absolute NDVI difference D_ndvi for the June–August calibration pair in Juye. Black points denote sampled observations and red lines denote fitted curves.

Accordingly, separate empirical response functions are specified for the two predictors. Their functional forms are selected to describe the observed monotonic relationships rather than being derived directly from the multiplicative decomposition in Equation (3). The two empirical response functions are written as:

$$\begin{cases} f_S(S\_ndvi) = a_1 \exp(-b_1 S\_ndvi) + c_1 \\ f_D(D\_ndvi) = a_2 \exp(-b_2 D\_ndvi) + c_2 \end{cases} \tag{4}$$

The coefficients a_1 and a_2 set the response amplitudes, b_1 and b_2 control the rates of change with the predictors, and c_1 and c_2 are empirical offsets. For positive amplitudes and positive decay coefficients, each function decreases with its predictor. For

empirical prediction, the two fitted response functions are combined using a weighted additive formulation:

$$\hat{\gamma}(S, D) = d_1 f_S(S\_ndvi) + d_2 f_D(D\_ndvi) \quad (5)$$

where d_1 and d_2 are empirically estimated combination coefficients. The additive form is a modeling choice adopted to integrate the complementary information contained in NDVI sum and NDVI difference. It is not an algebraic consequence of the multiplicative decorrelation decomposition in Equation (3), and the two response functions should not be interpreted as direct measurements of independent physical decorrelation components. Therefore, the proposed model is described as a physically motivated empirical model rather than a fully derived physical model. Its suitability is assessed through predictive performance over all valid pixels in the Juye area and through independent validation in the Gu'an area.

To select an appropriate conventional benchmark, linear, power-law, and exponential formulations based on a single-date NDVI predictor were first evaluated under the controlled simulation described in Section 4.1. The three candidate models were fitted and evaluated using the same simulated training and test populations. Among them, the single-NDVI exponential model produced the lowest prediction error and was consequently selected as the representative conventional model for the subsequent real-data comparison.

The selected single-NDVI exponential benchmark is written as:

$$\hat{\gamma}_{single}(x) = a_3 \exp(-b_3 x) + c_3 \quad (6)$$

Here, x denotes the single date NDVI used by the benchmark, and a_3, b_3 and c_3 are fitted coefficients. Figure 6 shows the corresponding relationship in the calibration samples. The fitted curve decreases and is approximately linear over much of the displayed NDVI range. In contrast to Equation (6), the joint model explicitly includes the change between the two acquisition dates through *D_ndvi*. The exponential forms alone do not guarantee predictions within [0, 1]; the admissible prediction range also depends on the coefficients and the predictor domain.

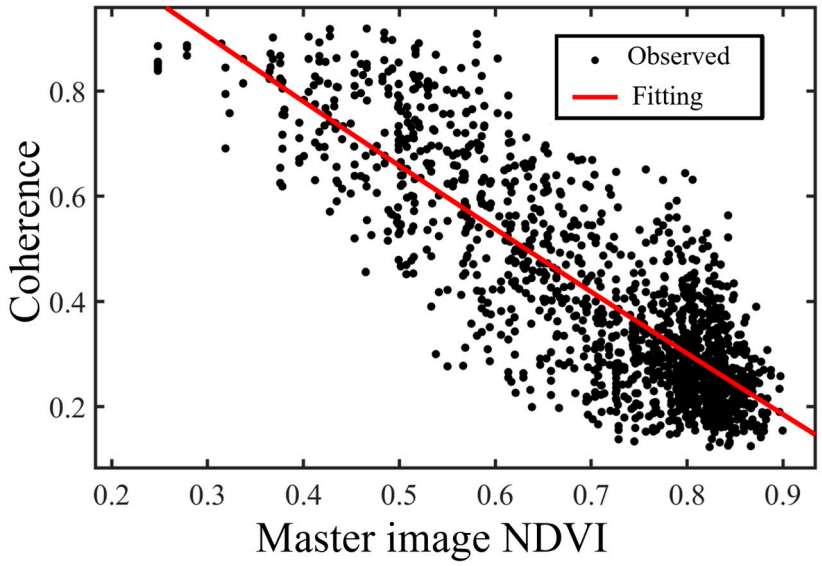


Figure 6. Observed coherence and the fitted single-NDVI exponential benchmark for the June–August calibration pair in Juye.

3.3. Model Parameter Estimation

Parameter estimation proceeds in two stages using the correlation-screened calibration samples from the June–August interferometric pair in the Juye area. First, the response functions defined in Section 3.2 are fitted to the corresponding predictor-specific calibration samples constructed in Section 3.1. The fitted component coefficients are then held fixed while the two combination weights are estimated. Importantly, the eight reported coefficients are never jointly estimated in a single optimization. The single-NDVI benchmark is fitted separately using samples selected according to the same window size and correlation-threshold magnitude and does not enter the weight-estimation stage.

In the first stage, each response function is fitted to its corresponding sample set. Let I_1, I_2 and I_3 denote the samples selected for the NDVI sum, the NDVI difference and the single-NDVI benchmark, respectively. Under a least squares criterion, the coefficients are estimated by

$$\theta_j = \mathrm{argmin}_{\theta_j} \sum_{i \in I_j} \left[\gamma_i - f_j(X_{j,i}; \theta_j)\right]^2, j = 1, 2, 3 \quad (7)$$

Here, $\theta_j = (a_j, b_j, c_j)$, and γ_i is the observed coherence. For j = 1, 2 and 3, the predictor X_j, i is the NDVI sum, the absolute NDVI difference and the single date NDVI, respectively; f_j denotes the corresponding response function in Equation (4) or Equation (6). This step is nonlinear because the decay coefficient b_j appears inside the exponential function.

In the second stage, the fitted NDVI sum and NDVI difference functions are evaluated on a common calibration set I_w. Every pixel in this set has both NDVI predictors and a coherence observation for the same SAR image pair. The two fixed component predictions at pixel i are denoted by

$$u_i = f_S(S\_ndvi_{,i}), v_i = f_D(D\_ndvi_{,i}) \quad (8)$$

The combination weights are then chosen to minimize the difference between the observed coherence and the weighted component predictions:

$$(\hat{d_1}, \hat{d_2}) = \mathrm{argmin}_{d_1, d_2} \sum_{i \in I_w} [\gamma_i - d_1 u_i - d_2 v_i]^2 \quad (9)$$

With u_i and v_i fixed, Equation (9) is a linear least squares problem in d1 and d2. Therefore, possible scale trade-offs between the component amplitudes and the combination weights do not constitute free directions in the second-stage optimization, because all component-function coefficients have already been fixed. The two columns of the design matrix contain ui and vi, and the response is γi. No independently fitted intercept is specified in Equation (5): its constant contribution is d1c1 + d2c2, determined by the fixed component offsets and the estimated weights. All component coefficients remain unchanged during this stage.

Table 2 lists the component coefficients and combination weights of the joint model, and Table 3 lists the coefficients of the single-NDVI benchmark. After estimation from the screened Juye calibration samples, all coefficients are held fixed. The fitted models are then applied to all valid pixels over the complete Juye area and subsequently transferred directly to the Gu'an validation area. No Gu'an observations are used for parameter estimation or model recalibration.

Table 2. Coefficients of the joint empirical coherence model.

Parameters	a_1	b_1	c_1	a_2	b_2	c_2	d_1	d_2
Values	2.6776	0.6633	−1.2668	0.5778	0.6637	−0.0694	0.1704	0.3508

Table 3. Coefficients of the single-NDVI benchmark.

Parameters	a_3	b_3	c_3
Values	9.6070	0.1334	−8.3540

4. Results

4.1. Monte Carlo Simulation and Benchmark Selection

A controlled Monte Carlo experiment was conducted to select the strongest conventional single-date NDVI benchmark and to compare it with PICM. The experiment evaluates predictive behavior under controlled conditions and is not intended as an independent physical validation of the proposed model.

Synthetic master- and secondary-date NDVI values were generated from a mixture distribution representing relatively sparse and dense vegetation conditions. The magnitude of inter-acquisition vegetation change was drawn independently and was randomly assigned a positive or negative direction to represent both vegetation greening and senescence. The resulting NDVI values were restricted to the interval [0.02, 0.99]. For each synthetic pixel, the NDVI sum and absolute NDVI difference were calculated as $S = NDVI_m + NDVI_s$ and $D = |NDVI_m - NDVI_s|$ respectively. The conventional single-date models used $x = \mathrm{NDVI}_m$ as their only predictor; therefore, x represents NDVI from one acquisition date rather than the mean of the two dates.

Reference coherence was generated using the following prescribed multiplicative function, which was motivated by the conventional coherence-composition framework:

$$\gamma_{\text{true}} = \gamma_\infty + (1 - \gamma_\infty)\exp[-(\alpha S + \beta D)] \tag{10}$$

This data-generating function depends on both the overall vegetation condition and the magnitude of vegetation change. It is deliberately different from the weighted additive formulation of PICM and therefore does not assume that the proposed empirical model is the true generating model. To approximate finite-look coherence estimation, a positive bias of $(1 - \gamma_{\text{true}})/(2L)$ and zero-mean Gaussian noise with a standard deviation of $(1 - \gamma_{\text{true}}^2)/(\sqrt{2L})$ were added, where L denotes the number of looks. Simulated observed coherence was then restricted to the interval [0.02, 0.999]. Independent training and test populations containing 4000 pixels each were generated with $L = 20$. The training population was used for parameter estimation, whereas predictive errors were calculated against the noise-free reference coherence in the independent test population.

Three conventional single-date NDVI candidates were considered: a linear model, a two-parameter power-law model, and a three-parameter exponential model. They were defined as

$$\begin{cases} \hat{y}_{\text{linear}}(x) = \beta_0 + \beta_1 x \\ \hat{y}_{\text{power}}(x) = a_P x^{b_P} \\ \hat{y}_{\text{exponential}}(x) = a_E \exp(-b_E x) + c_E \end{cases} \tag{11}$$

All three conventional candidates were fitted to the same training population. The linear model was estimated by ordinary least squares, whereas the power-law and exponential models were estimated by nonlinear least squares. PICM was estimated using the two-stage procedure in Section 3.3, so its eight coefficients were not optimized jointly. Performance was assessed using RMSE, MAE, bias, and R^2 on the independent test population, while AIC and BIC were calculated from the common training population to penalize model complexity.

Figure 7 summarizes the simulation design. True coherence varies jointly with S and D (Figure 7a). When the master-date NDVI is fixed but the secondary-date NDVI changes,

true coherence also changes (Figure 7b), whereas a single-date model must assign the same prediction. Figure 7c shows the three conventional functions fitted to identical training observations.

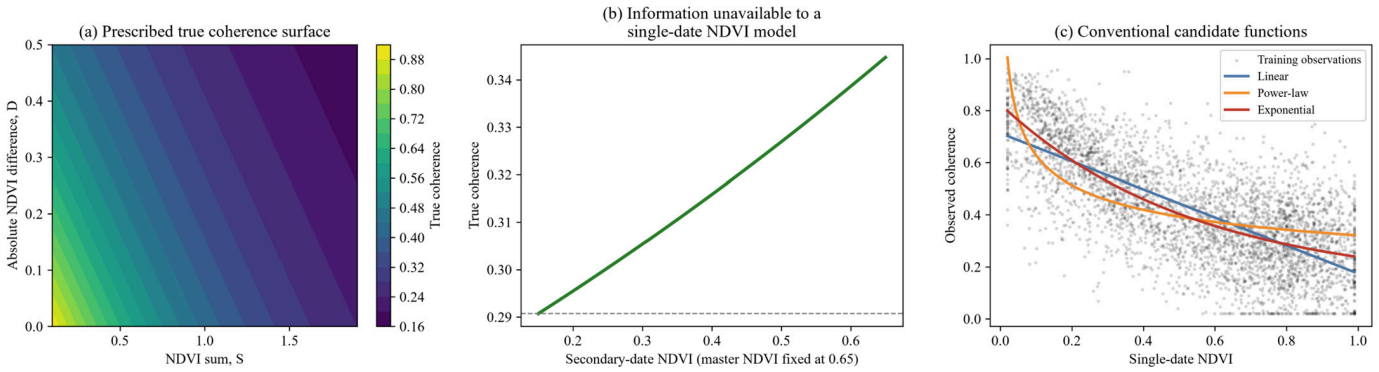


Figure 7. Synthetic data-generating process and conventional single-date NDVI candidate models. (**a**) Prescribed true coherence surface as a function of the NDVI sum S and absolute NDVI difference D; (**b**) variation in true coherence when the master-date NDVI is fixed at 0.65 and the secondary-date NDVI varies, illustrating information unavailable to a model using only the master-date NDVI; and (**c**) linear, power-law, and exponential functions fitted to the same single-date NDVI training observations.

The candidate-model results are shown in Figure 8 and Table 4. The exponential model achieved the lowest conventional-model RMSE (0.0598) and MAE (0.0408), the highest R^2 (0.875), and the lowest AIC and BIC. It was therefore selected as the representative single-NDVI benchmark. No Gu'an observations were used in this selection.

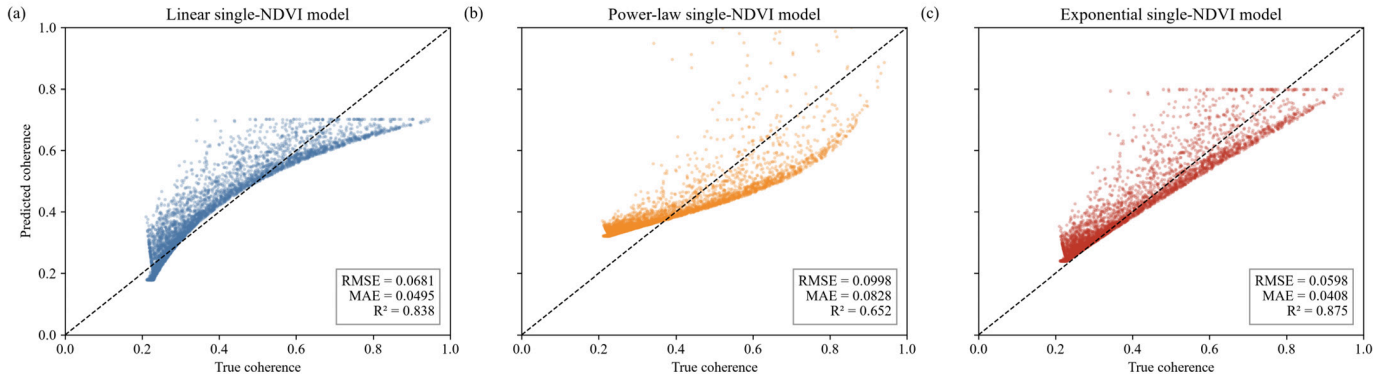


Figure 8. Predicted versus true coherence for the conventional single-date NDVI candidates in the independent synthetic test population. (**a**) Linear model; (**b**) power-law model; and (**c**) exponential model. All models were fitted using the same training population and evaluated using the same independent test population.

Table 4. Performance of the candidate conventional models and PICM in the Monte Carlo experiment.

Model	Parameters	RMSE	MAE	Bias	R^2	AIC	BIC
Linear single-NDVI	2	0.0681	0.0495	0.0169	0.838	−15,500.55	−15,487.96
Power-law single-NDVI	2	0.0998	0.0828	0.0198	0.652	−14,788.98	−14,776.39
Exponential single-NDVI	3	0.0598	0.0408	0.0159	0.875	−15,755.80	−15,736.92
PICM	8	0.0415	0.0342	0.0178	0.940	−16,167.48	−16,117.13

PICM was then compared with the selected exponential model (Figure 9). PICM reduced RMSE from 0.0598 to 0.0415 (30.6%) and MAE from 0.0408 to 0.0342, while R^2 increased from 0.875 to 0.940. Its AIC and BIC were also lower despite the larger parameter count, indicating that the improvement was not solely due to unpenalized model complexity.

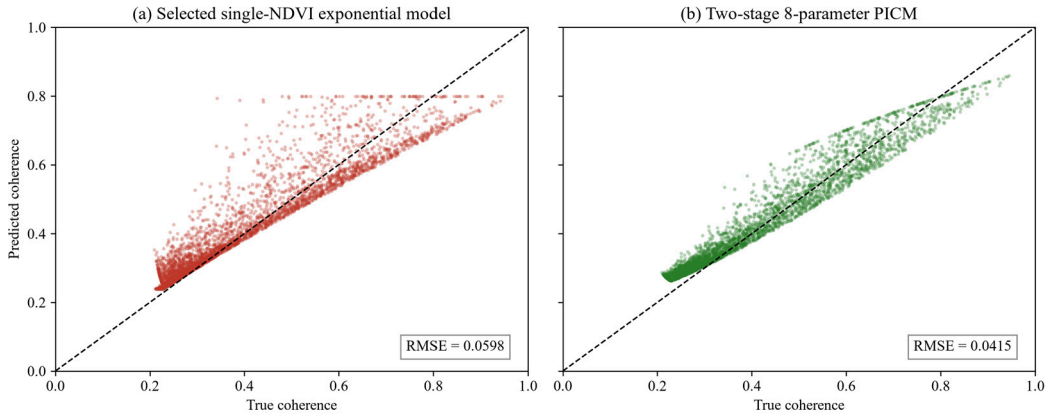


Figure 9. Predicted versus true coherence in the independent synthetic test population. (**a**) The selected single-NDVI exponential benchmark; and (**b**) the proposed two-stage eight-parameter PICM. The dashed line denotes the 1:1 reference.

The experiment therefore identifies the exponential formulation as the strongest conventional single-date benchmark and shows that PICM can additionally represent information associated with inter-acquisition vegetation change. Because the results depend on a prescribed synthetic process, they are interpreted as internal numerical evidence; independent spatial validation with real Sentinel-1 and Landsat observations is presented in Section 4.3.To further assess model stability, we conducted robustness and evaluation-pixel selection tests (Figure 10). As shown in Figure 10a, the PICM consistently achieves lower RMSE than the selected single-NDVI exponential model across different multi-looking conditions (8, 12, 20, and 40 looks). Additionally, Figure 10b demonstrates that the PICM maintains reliable predictive performance whether evaluated on all valid pixels or only on the correlation-screened subset.

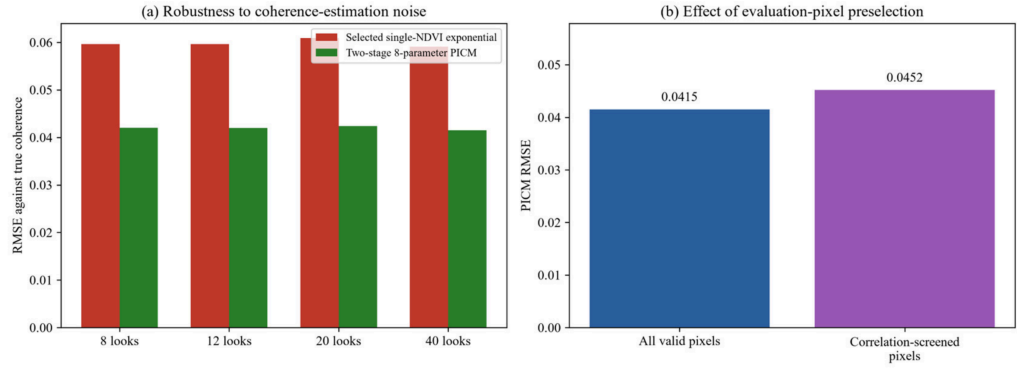


Figure 10. Robustness and evaluation-pixel selection tests. (**a**) RMSE of the selected single-NDVI exponential model and PICM across different numbers of looks; and (**b**) PICM RMSE calculated using all valid pixels and the correlation-screened subset. Model coefficients were held fixed in both tests.

4.2. Model Calibration and Full-Area Prediction in the Juye Area

The June–August interferometric pair in the Juye area, during which vegetation growth and inter-acquisition vegetation changes were pronounced, was selected as the calibration period. Model parameters were estimated using the correlation-screened samples described

in Section 3.1. After parameter estimation, the fitted coefficients were held fixed and applied to all valid pixels over the complete Juye area without further correlation-based screening. A full-area comparison was then conducted between the proposed model based on NDVI sum and NDVI difference and the traditional single-NDVI model. Because the June–August data contributed to parameter estimation, the results for this period represent full-area prediction during the calibration period rather than independent validation. As shown in Figure 11b,c, the coherence estimated by the proposed model is generally consistent with the actual coherence in both urban built-up areas and vegetation covered areas. The difference image, obtained by subtracting the estimated coherence from the true coherence, is shown in Figure 11d. It can be observed that the errors are randomly distributed with no apparent systematic trend. Relatively larger errors are primarily concentrated in urban areas. This can be attributed to the low vegetation coverage in these areas, where NDVI is not the primary factor affecting coherence. As shown in Figure 11e, the coherence estimated by the single-NDVI model is also generally consistent with the actual coherence in some areas. However, compared with the proposed model, considerable discrepancies exist between the estimated and true coherence values in vegetated areas. Figure 11f similarly shows that relatively larger errors are concentrated in urban areas.

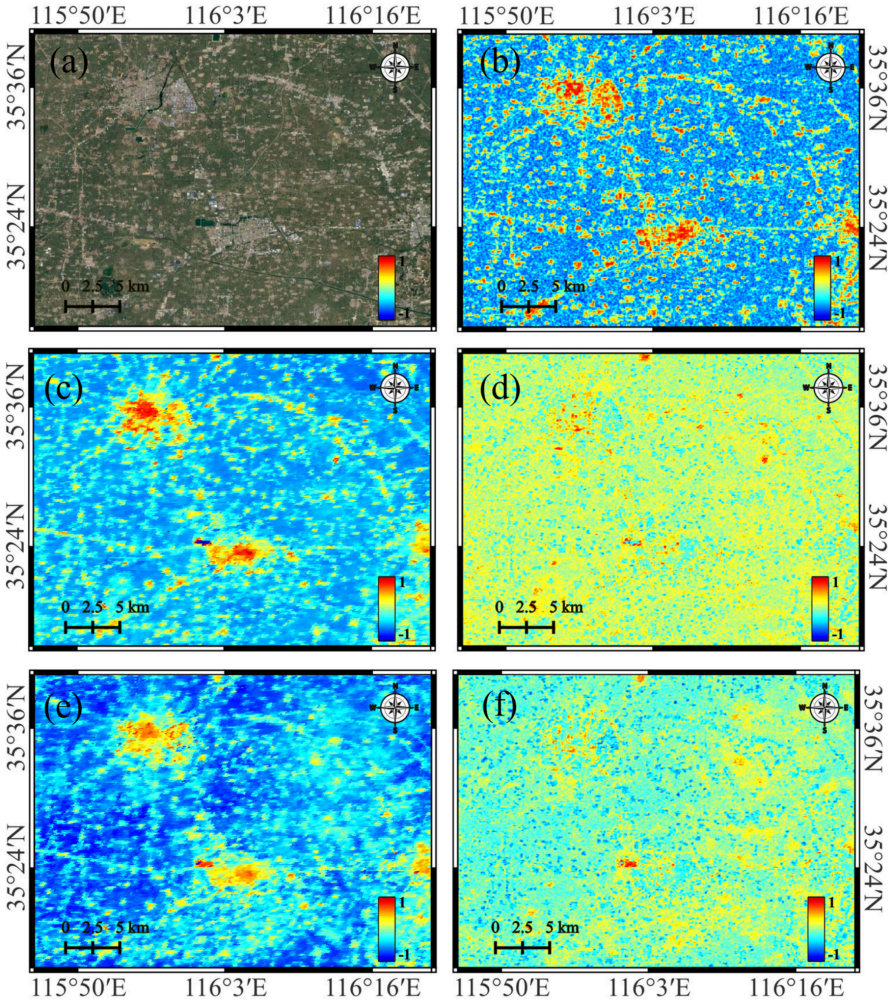


Figure 11. Full-area prediction results for the June–August calibration period in the Juye area. Model parameters were estimated using correlation-screened calibration samples, whereas the prediction maps include all valid pixels without correlation-based preselection. (**a**) Optical image of the Juye area; (**b**) observed coherence; (**c**) coherence predicted by the proposed model; (**d**) corresponding prediction error; (**e**) coherence predicted by the single-NDVI model; and (**f**) corresponding prediction error.

As shown in Figure 12, the errors of both models approximately follow a Gaussian distribution and are mainly concentrated within the range of −0.2 to 0.2. The error distributions and summary statistics are calculated using all valid pixels over the complete Juye area rather than only the correlation-screened calibration samples. The mean error of the vegetation change aware coherence model is 0.035, while that of the single-NDVI model is −0.116, further reflecting the difference in error distribution between the two. These results indicate that the model calibrated using the correlation-screened samples can reproduce the spatial coherence pattern over the complete Juye area, including pixels not retained during calibration. The relatively small mean error suggests a limited overall prediction bias during the calibration period. Moreover, the proposed model provides better full-area prediction performance than the single-NDVI benchmark, particularly in vegetated areas. Because the June–August observations contributed to parameter estimation, independent spatial validation is conducted separately using the Gu'an area in Section 4.3. This improvement is mainly attributed to the fact that NDVI sum and NDVI difference more comprehensively capture vegetation dynamics and cover levels between the acquisition dates of the master and slave images, thereby exhibiting stronger statistical correlation with SAR coherence.

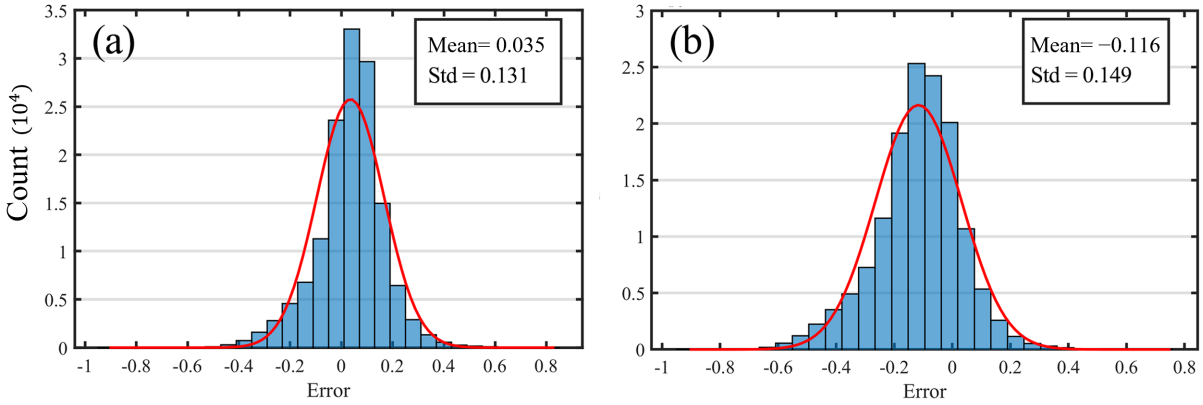


Figure 12. Error histograms for the Juye area: (**a**) errors of the proposed model; (**b**) errors of the exponential function model.

To further evaluate the predictive capability of the model across different months of the year, we used the proposed model to make predictions for various months and compared the results with those from the single-NDVI model. As shown in Figure 13, the coherence estimated by the PICM model in vegetated areas is generally consistent with the actual coherence across all months. The agreement is closest during the growing season, while model performance is relatively weaker during the non-growing season. This can be attributed to sparse vegetation and low vegetation coverage during the non-growing season, where NDVI values are generally low and vegetation changes are minimal. Under such conditions, NDVI is no longer the dominant factor affecting actual coherence in the area. In contrast, the single-NDVI model performs considerably worse than the proposed model in predicting coherence over vegetated areas for most months, particularly during April to August when vegetation grows rapidly and canopy coverage is dense. This is mainly because during the growing season, vegetation changes quickly and coverage is high, leading to a significant influence on coherence. The single NDVI metric alone fails to adequately capture such rapid vegetation dynamics and cover levels.

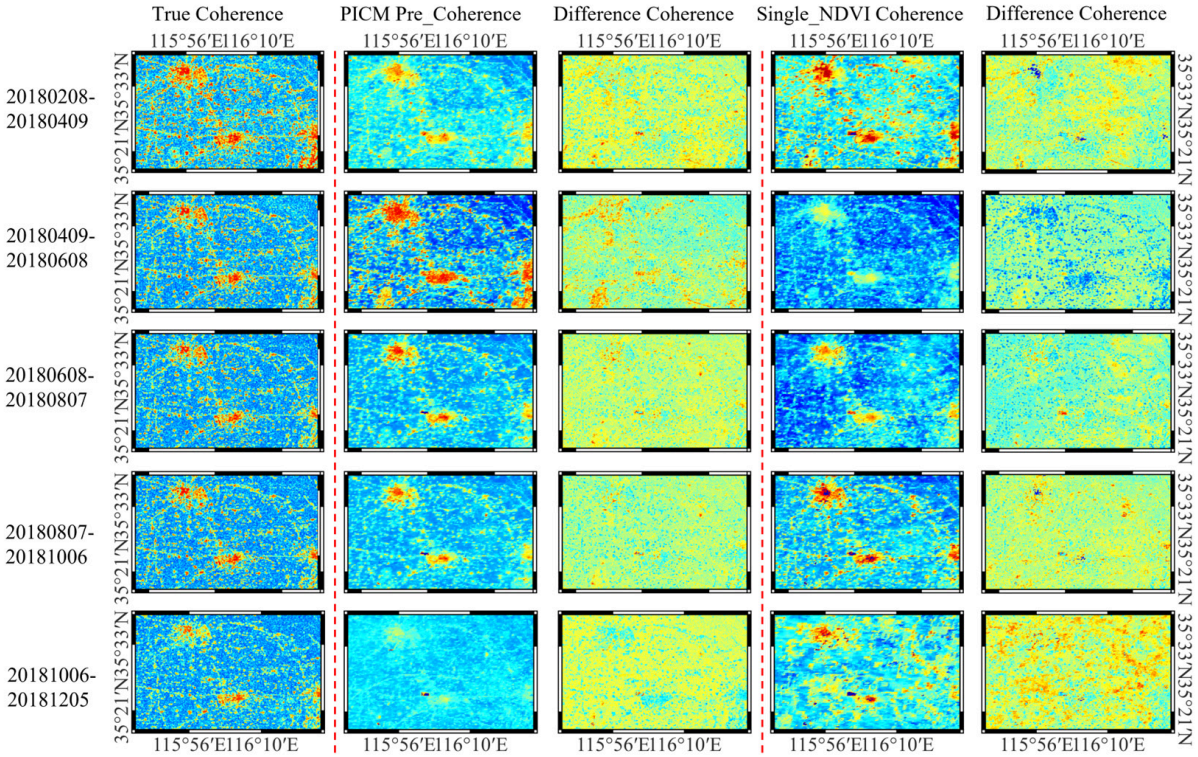


Figure 13. Prediction performance of different months in the Juye area.

4.3. Independent Spatial Validation in the Gu'an Area

To independently evaluate the spatial transferability of the proposed model, the coefficients estimated from the correlation-screened calibration samples in the Juye area were transferred directly to the Gu'an area. The SAR and optical data in Gu'an were processed using the same preprocessing and coregistration procedures as those used in Juye; however, no Gu'an observations were used for calibration-sample selection, parameter estimation, parameter adjustment, or model selection. The transferred models were applied to all valid pixels in Gu'an without correlation-based preselection. As shown in Figure 14b,c, the coherence predicted by the proposed model closely resembles the observed coherence in the vegetated areas of Gu'an. The spatially distributed prediction errors are generally random, although they are slightly larger than those obtained in the Juye area.

As shown in Figure 15, these differences still approximately follow a Gaussian distribution and are mainly concentrated within the range of −0.4 to 0.4, indicating that the proposed model is reasonable. Similarly, Figure 14e shows that the coherence estimated by the single-NDVI model also closely resembles the true coherence in some vegetated areas, but the errors are larger for vegetated regions. As shown in Figure 15a,b, the mean error of the vegetation change aware coherence model is −0.048, while that of the exponential model is 0.089. For the Gu'an area, the proposed model achieves smaller errors and provides more accurate predictions.

To evaluate the generalizability of the proposed model in the Gu'an area across the entire year, we compared the proposed model with the single-NDVI index model across different months, as shown in Figure 16. When vegetation coverage is low, the prediction performance of the two models shows little difference. However, during the growing season when vegetation coverage is high, the prediction accuracy of the proposed model is higher compared with that in the non-growing season. Comparing the model prediction performance between the Juye area and the Gu'an area, it can be observed that the prediction accuracy is higher in the Juye area, indicating that the model has certain limitations. Based on the experimental results described above, it can be concluded that

the PICM model achieves higher prediction accuracy, better seasonal adaptability, and a certain degree of spatial transferability compared with the single-NDVI index model.

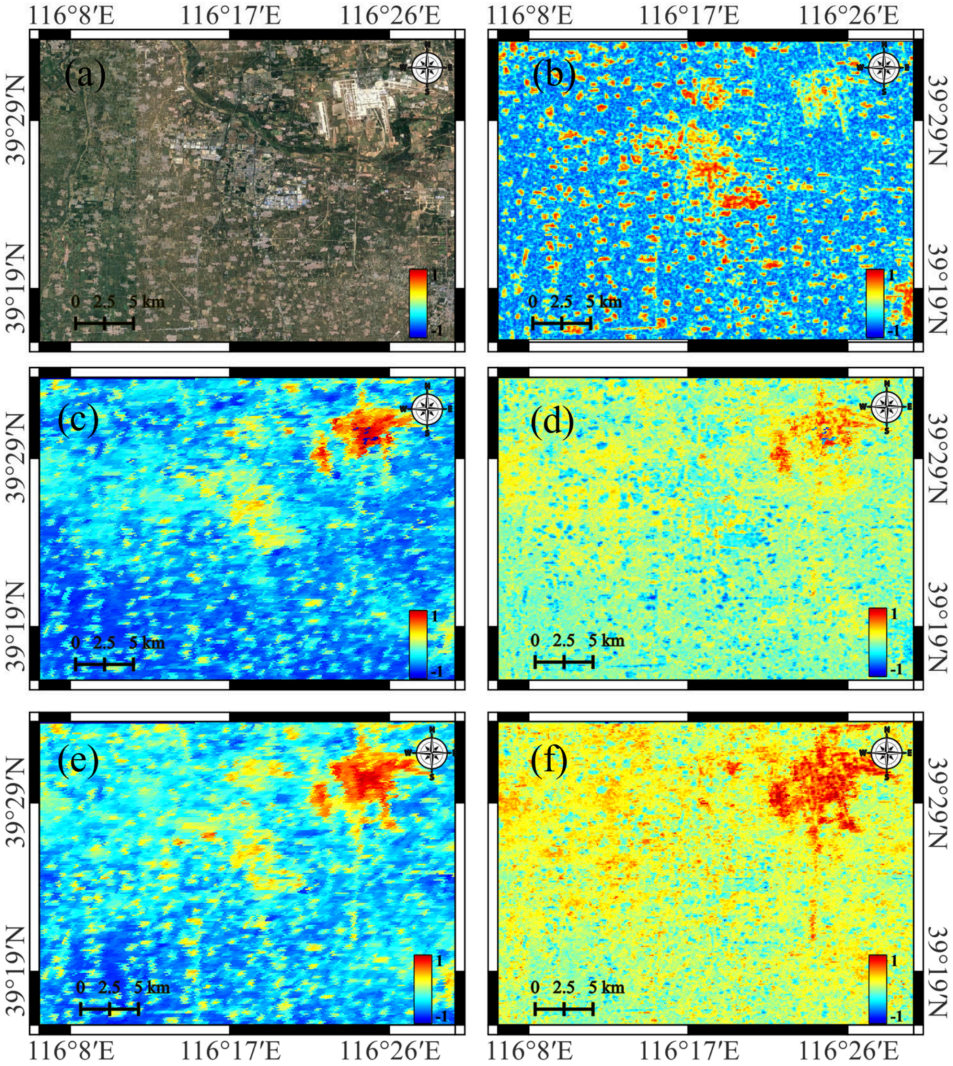


Figure 14. Gu'an area (June–August). (**a**) Satellite image of the Gu'an area; (**b**) true coherence image; (**c**) coherence estimation result of the proposed model; (**d**) corresponding difference image; (**e**) coherence estimation result of the exponential function model; (**f**) corresponding difference image.

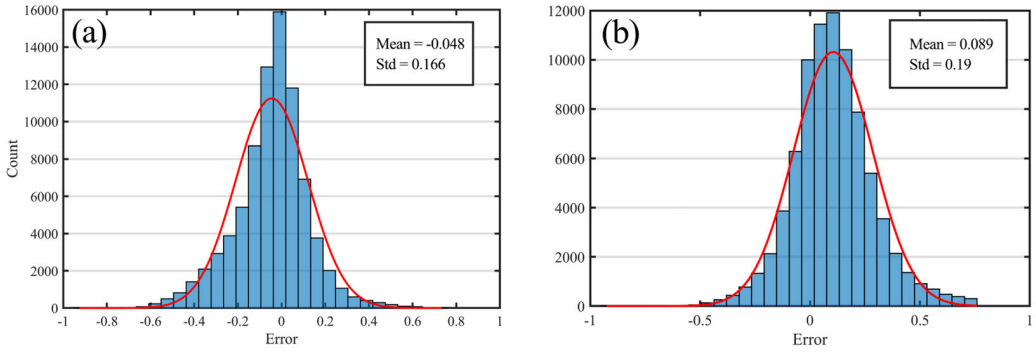


Figure 15. Error histograms: (**a**) errors of the proposed model; (**b**) errors of the exponential function model.

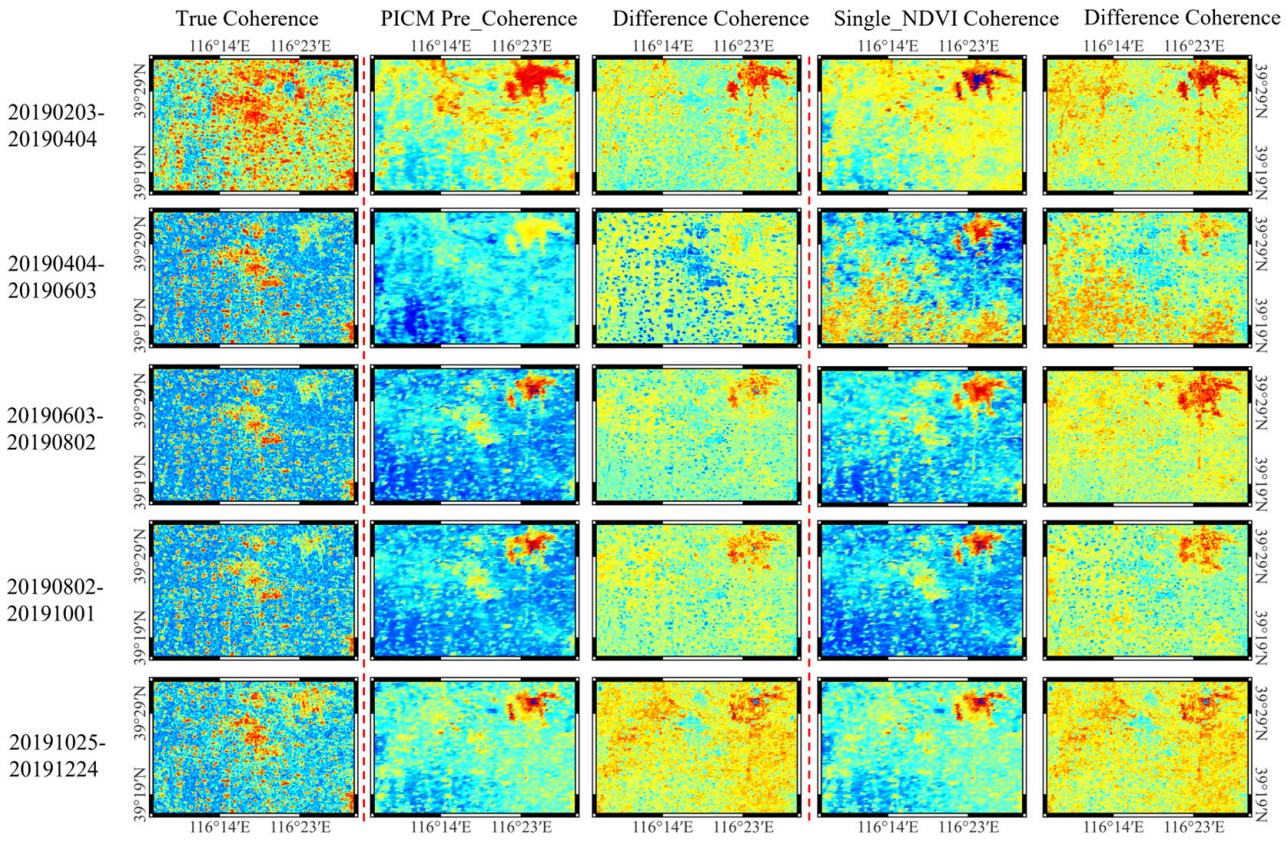


Figure 16. Prediction performance of different months in the Gu'an area.

5. Discussion

5.1. Constraints on Spatial Transferability and Temporal-Baseline Applicability

The proposed coherence estimation model, which integrates the NDVI sum and absolute NDVI difference, achieved lower prediction errors than the conventional single-NDVI model for the approximately 60-day interferometric pairs examined. Previous studies have reported negative or nonlinear relationships between vegetation coverage and interferometric coherence [18,28,29]. Crop-monitoring studies have further shown that coherence generally decreases during crop growth, reaches low values when canopy cover is greatest, and increases again after harvesting [30]. These findings are consistent with the seasonal patterns observed in this study. However, most previous NDVI-based models primarily characterize vegetation conditions using NDVI from a single acquisition. Such models cannot explicitly represent vegetation changes between the two SAR acquisitions and may therefore perform poorly during periods of rapid vegetation development. By incorporating both overall vegetation conditions and inter-acquisition vegetation change, the proposed model showed a more pronounced improvement over the single-NDVI model during the growing season.

Although the PICM performed better than the single-NDVI model in both study areas, its prediction accuracy was lower in Gu'an than in Juye. This difference highlights the difficulty of transferring empirical coherence models between regions. Although both areas are located in the North China Plain and are dominated by farmland, differences in surface conditions, agricultural practices, phenology, and non-vegetation disturbances can alter the relationship between NDVI-derived predictors and interferometric coherence.

First, land-surface heterogeneity and local surface processes constrain model transferability. Differences in farming practices and microtopography between the two regions may affect crop development and radar scattering characteristics [31]. During the study period,

large-scale infrastructure projects, including the Jingde Expressway and the Airport North Line Expressway, were under construction in the Gu'an area. These activities may produce surface disturbances and changes in radar scatterers that are unrelated to vegetation [32]. Such disturbances can rapidly alter the dielectric and geometric properties of the land surface, resulting in coherence loss that cannot be represented by NDVI alone [33]. This confirms that observed interferometric coherence is an integrated response to multiple surface processes rather than a function of vegetation conditions alone.

Second, regional differences in climate, crop type, and phenological timing may affect the relationship between vegetation and coherence. Although both regions have a temperate monsoon climate, differences in hydrothermal conditions and cropping practices can lead to variations in vegetation growth rates, biomass accumulation, and phenological stages. Precipitation and temperature are important controls on NDVI dynamics [34,35], while previous studies have shown that the relationship between coherence and vegetation development can vary among crop types and acquisition configurations [36,37]. The NDVI sum and difference capture vegetation conditions and their changes, but they do not explicitly represent regional phenological backgrounds or meteorological disturbances. These differences may therefore reduce prediction accuracy when the calibrated model is transferred to another region.

Third, land-cover composition affects the availability of vegetation-sensitive calibration samples. As shown in Figure 17, the number of pixels satisfying the correlation threshold varies among interferometric periods, although the numbers retained using the NDVI sum and difference are generally higher than those obtained using single-date NDVI. During the non-growing season, vegetation cover and inter-acquisition vegetation changes are limited, reducing the explanatory power of NDVI for coherence variations. Consequently, fewer vegetation-sensitive samples are available, which may reduce the robustness of parameter estimation [38]. The counts shown in Figure 17 are used only to diagnose seasonal variations in vegetation sensitivity; correlation-based screening is not applied during full-area prediction or independent validation.

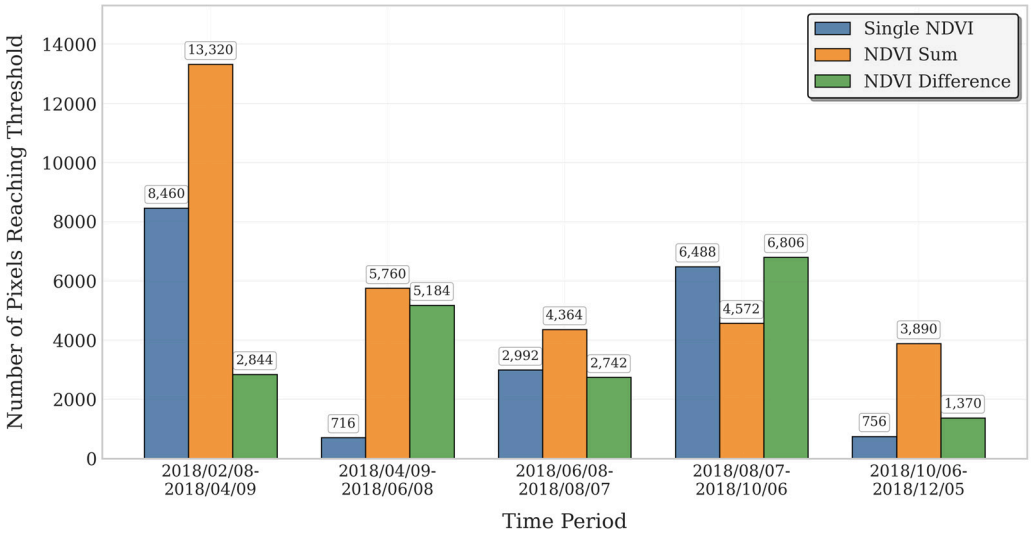


Figure 17. Number of valid pixels meeting the correlation threshold across different time periods.

In addition to spatial transferability, the applicability of the model is constrained by temporal baseline. All experiments in this study used interferometric pairs with an approximately 60-day baseline; therefore, the results do not establish model performance for other temporal separations. Previous studies have shown that the information provided by coherence varies with temporal baseline, polarization, crop type, and acquisition geome-

try [21,37]. For shorter baselines, such as 12, 24, or 36 days, vegetation changes between acquisitions may be smaller, potentially reducing the contribution of the NDVI-difference predictor. Conversely, longer baselines may increase the influence of other decorrelation mechanisms. Future work should therefore evaluate the model across multiple temporal baselines and determine whether baseline-specific or crop-specific calibration is required.

5.2. Limitation Analysis

Although the PICM model demonstrates potential, it has inherent limitations as an empirical model [39]. First, its generalizability across different regions and land cover types requires systematic validation. This study was conducted only in agricultural areas of the North China Plain. The model's performance in other typical landforms (e.g., mountainous or hilly terrain), other dominant vegetation types (e.g., forests, shrubs, wetlands), or different climatic zones (e.g., tropical or arid regions) remains unknown. Forests possess more complex vertical structures, and their interaction with C-band signals is considerably more intricate [40]; thus, a simple NDVI metric may not adequately characterize such complexity. In mountainous areas, terrain induced geometric distortions, shadowing, and layover can severely interfere with coherence, and their influence may far exceed that of vegetation changes [41].

Second, the model lacks sufficient capability to decouple and quantify the coupled effects of multiple factors. Temporal coherence is the result of the combined influence of various land surface and atmospheric processes, including vegetation, soil moisture, surface temperature, precipitation, wind, and even surface deformation. Although this study focuses on the dominant role of vegetation factors by constructing NDVI difference and NDVI sum to link coherence with NDVI variations, it does not explicitly isolate or quantify the independent contributions of other factors [42]. For instance, rapid changes in soil moisture can significantly alter the surface dielectric constant, inducing decorrelation unrelated to vegetation dynamics [43,44]; intense precipitation events and wind disturbances can also directly affect radar signal scattering characteristics. Consequently, the model's predictive performance may exhibit considerable fluctuations in scenarios dominated by non-vegetation factors, such as after rainfall, during snowmelt periods, or following strong winds. Future models could consider integrating multi source data—such as satellite derived soil moisture, meteorological precipitation and wind speed data—or incorporating auxiliary indicators that characterize surface microwave scattering properties, such as surface roughness derived from SAR data [45]. This would enable the development of a multi factor collaborative estimation model, thereby enhancing model robustness and generalizability under complex environmental conditions.

In summary, the PICM model developed in this study significantly enhances the predictive capability for InSAR coherence in agricultural areas by incorporating a dynamic perspective on vegetation change, thereby providing a superior tool for assessing time-series InSAR data quality in densely vegetated regions. However, the regional discrepancies and model limitations revealed in the Section 5 highlight the complexity of InSAR decorrelation mechanisms. Future efforts should focus on developing advanced models that are more physically grounded, capable of integrating multi source observations, and designed to account for spatial heterogeneity. Such models would ultimately enable more accurate prediction and mitigation of InSAR decorrelation noise over large areas and under complex environmental conditions, further unlocking the potential of time-series InSAR for global surface deformation monitoring.

6. Conclusions

This study developed a dual-NDVI empirical coherence model (PICM) that uses the sum and absolute difference of the NDVI values from the two SAR acquisition dates to characterize overall vegetation conditions and inter-acquisition vegetation change, respectively. The model was calibrated in the Juye area and subsequently transferred to the Gu'an area without recalibration. In the independent Gu'an validation, the PICM achieved an error standard deviation of 0.166 and a mean error of −0.048, compared with 0.190 and 0.089 for the conventional single-NDVI model, respectively. These results demonstrate that incorporating vegetation conditions from both acquisition dates improves coherence prediction for the approximately 60-day interferometric pairs examined in this study.

The predicted coherence may provide prior information for interferometric-pair selection and network optimization in agricultural SBAS-InSAR applications. However, integration of the proposed model into an operational automatic interferogram-network selection workflow has not yet been implemented or validated. Further evaluation is required before extending the model to other temporal baselines and land-cover conditions.

Author Contributions: Conceptualization, G.L.; methodology, C.M.; software, C.M.; validation, C.M., S.L. and X.W.; formal analysis, C.M.; investigation, S.L. and X.W.; resources, G.L.; data curation, C.M.; writing—original draft preparation, C.M., S.L. and X.W.; writing—review and editing, C.M. and G.L.; visualization, C.M.; supervision, G.L.; project administration, G.L.; funding acquisition, G.L. All authors have read and agreed to the published version of the manuscript.

Funding: This work was jointly supported by the National Natural Science Foundation of China (Grants U22A20565 and 42371458), the Open Project Fund of National Engineering Research Center of Digital Construction and Evaluation Technology of Urban Rail Transit (No. 2025-035), and the Innovation Project of Technology Innovation Center for Emergency Surveying and Mapping, Ministry of Natural Resources (No. YJCX-2026-YB-08).

Data Availability Statement: The original Sentinel-1 SAR data and Landsat optical imagery analyzed in this study are publicly available from the European Space Agency (ESA) and the United States Geological Survey (USGS)/Alaska Satellite Facility (ASF), respectively. The processed datasets and models generated during this study are available on request from the corresponding author.

Conflicts of Interest: The authors declare no conflict of interest.

References

1. Massonnet, D.; Feigl, K.L. Radar interferometry and its application to changes in the Earth's surface. *Rev. Geophys.* **1998**, *36*, 441–500. [CrossRef]
2. Hu, J.; Li, Z.W.; Ding, X.L.; Zhu, J.; Zhang, L.; Sun, Q. Resolving three-dimensional surface displacements from InSAR measurements: A review. *Earth-Sci. Rev.* **2014**, *133*, 1–17. [CrossRef]
3. Sun, Q.; Zhang, L.; Ding, X.; Hu, J.; Liang, H. Investigation of slow-moving landslides from ALOS/PALSAR images with TCPInSAR: A case study of Oso, USA. *Remote Sens.* **2015**, *7*, 72–88. [CrossRef]
4. Qu, F.; Lu, Z.; Zhang, Q.; Bawden, G.W.; Kim, J.-W.; Zhao, C.; Qu, W. Mapping ground deformation over Houston–Galveston, Texas using multi-temporal InSAR. *Remote Sens. Environ.* **2015**, *169*, 290–306. [CrossRef]
5. Qu, W.; Zhang, B.; Lu, Z.; Kim, J.W.; Zhang, Q.; Gao, Y.; Hao, M.; Zhu, W.; Qu, F. Source parameter estimation of the 2009 Ms6. 0 Yao'an Earthquake, Southern China, using InSAR observations. *Remote Sens.* **2019**, *11*, 462. [CrossRef]
6. Xue, F.; Lv, X.; Dou, F.; Yun, Y. A review of time-series interferometric SAR techniques: A tutorial for surface deformation analysis. *IEEE Geosci. Remote Sens. Mag.* **2020**, *8*, 22–42. [CrossRef]
7. Ju, X.; Gao, S.; Li, Y. Polarimetric time-series InSAR for surface deformation monitoring in mining area using dual-polarization data. *Sensors* **2025**, *25*, 5968. [CrossRef]
8. Slatton, K.C.; Crawford, M.M.; Evans, B.L. Fusing interferometric radar and laser altimeter data to estimate surface topography and vegetation heights. *IEEE Trans. Geosci. Remote Sens.* **2002**, *39*, 2470–2482. [CrossRef]
9. Liang, H.; Zhang, L.; Ding, X.; Lu, Z.; Li, X.; Hu, J.; Wu, S. Suppression of Coherence Matrix Bias for Phase Linking and Ambiguity Detection in MTInSAR. *IEEE Trans. Geosci. Remote Sens.* **2021**, *59*, 1263–1274. [CrossRef]

10. Zhang, M.; Li, Z.; Tian, B.; Zhou, J.; Zeng, J. A method for monitoring hydrological conditions beneath herbaceous wetlands using multi-temporal ALOS PALSAR coherence data. *Remote Sens. Lett.* **2015**, *6*, 618–627. [CrossRef]
11. Ma, G.; Zhao, Q.; Wang, Q.; Liu, M. On the effects of InSAR temporal decorrelation and its implications for land cover classification: The case of the ocean-reclaimed lands of the Shanghai megacity. *Sensors* **2018**, *18*, 2939. [CrossRef]
12. Jung, J.; Kim, D.-J.; Lavalle, M.; Yun, S.-H. Coherent change detection using InSAR temporal decorrelation model: A case study for volcanic ash detection. *IEEE Trans. Geosci. Remote Sens.* **2016**, *54*, 5765–5775. [CrossRef]
13. Santoro, M.; Wegmuller, U.; Askne, J.I.H. Signatures of ERS–Envisat interferometric SAR coherence and phase of short vegetation: An analysis in the case of maize fields. *IEEE Trans. Geosci. Remote Sens.* **2009**, *48*, 1702–1713. [CrossRef]
14. Sedze, M.; Heggy, E.; Bretar, F.; Berveiller, D.; Jacquemoud, S. L-band InSAR Decorrelation Analysis in Volcanic Terrains Using Airborne LiDAR Data and in Situ Measurements: The Case of the Piton de La Fournaise Volcano, France. In *2012 IEEE International Geoscience and Remote Sensing Symposium*; IEEE: New York, NY, USA, 2012; pp. 3907–3910.
15. Arab-Sedze, M.; Heggy, E.; Bretar, F.; Berveiller, D.; Jacquemoud, S. Quantification of L-band InSAR coherence over volcanic areas using LiDAR and in situ measurements. *Remote Sens. Environ.* **2014**, *152*, 202–216. [CrossRef]
16. Nikaein, T.; Iannini, L.; Molijn, R.A.; Lopez-Dekker, P. On the value of Sentinel-1 InSAR coherence time-series for vegetation classification. *Remote Sens.* **2021**, *13*, 3300. [CrossRef]
17. Wang, C.; Fan, J.; Lin, S.; Rao, Y.; Huang, H. Study of the correlation between optical vegetation index and SAR data and the main affecting factors. *Remote Sens. Land Resour.* **2020**, *32*, 130–137.
18. Bai, Z.; Fang, S.; Gao, J.; Zhang, Y.; Jin, G.; Wang, S.; Zhu, Y.; Xu, J. Could vegetation index be derive from synthetic aperture radar?–the linear relationship between interferometric coherence and NDVI. *Sci. Rep.* **2020**, *10*, 6749. [CrossRef]
19. Liao, T.H.; Simard, M.; Denbina, M.; Lamb, M.P. Monitoring water level change and seasonal vegetation change in the coastal wetlands of louisiana using L-band time-series. *Remote Sens.* **2020**, *12*, 2351. [CrossRef]
20. Pulella, A.; Aragão Santos, R.; Sica, F.; Posovszky, P.; Rizzoli, P. Multi-temporal sentinel-1 backscatter and coherence for rainforest mapping. *Remote Sens.* **2020**, *12*, 847. [CrossRef]
21. Mestre-Quereda, A.; Lopez-Sanchez, J.M.; Vicente-Guijalba, F.; Jacob, A.W.; Engdahl, M.E. Time-series of Sentinel-1 interferometric coherence and backscatter for crop-type mapping. *IEEE J. Sel. Top. Appl. Earth Obs. Remote Sens.* **2020**, *13*, 4070–4084. [CrossRef]
22. Liu, Z.Y.; Zhang, C.; Liu, Z.K.; Yuan, J.J.; Qi, H.C.; Pan, Y.F.; Zhu, H.L.; Wu, X.W.; Wang, H. Empirical relationship between radar coherence and NDVI. *Bull. Surv. Mapp.* **2021**, 45.
23. Cao, Y.; Li, P.; Hao, D.; Lian, Y.; Wang, Y.; Zhao, S. Analysis of the relationship between vegetation and radar interferometric coherence. *Sustainability* **2022**, *14*, 16471. [CrossRef]
24. Lavalle, M.; Hensley, S. Extraction of structural and dynamic properties of forests from polarimetric-interferometric SAR data affected by temporal decorrelation. *IEEE Trans. Geosci. Remote Sens.* **2015**, *53*, 4752–4767. [CrossRef]
25. Torres, R.; Snoeij, P.; Geudtner, D.; Bibby, D.; Davidson, M.; Attema, E.; Potin, P.; Rommen, B.; Floury, N.; Brown, M.; et al. GMES Sentinel-1 mission. *Remote Sens. Environ.* **2012**, *120*, 9–24. [CrossRef]
26. Yague-Martinez, N.; Prats-Iraola, P.; Gonzalez, F.R.; Brcic, R.; Shau, R.; Geudtner, D.; Eineder, M.; Bamler, R. Interferometric processing of Sentinel-1 TOPS data. *IEEE Trans. Geosci. Remote Sens.* **2016**, *54*, 2220–2234. [CrossRef]
27. Liu, H.Q.; Huete, A. A feedback based modification of the NDVI to minimize canopy background and atmospheric noise. *IEEE Trans. Geosci. Remote Sens.* **1995**, *33*, 457–465. [CrossRef]
28. Chen, Y.; Sun, Q.; Hu, J. Quantitatively estimating of InSAR decorrelation based on Landsat-derived NDVI. *Remote Sens.* **2021**, *13*, 2440. [CrossRef]
29. Pan, J.; Zhao, R.; Xu, Z.; Cai, Z.; Yuan, Y. Quantitative estimation of sentinel-1A interferometric decorrelation using vegetation index. *Front. Earth Sci.* **2022**, *10*, 1016491. [CrossRef]
30. Xu, W.C. A review on correlation coefficients. *J. Guangdong Univ. Technol.* **2012**, *29*, 12–17.
31. Li, J.; Lei, H. Tracking the spatio-temporal change of planting area of winter wheat-summer maize cropping system in the North China Plain during 2001–2018. *Comput. Electron. Agric.* **2021**, *187*, 106222. [CrossRef]
32. Hu, B.; Chen, J.; Zhang, X. Monitoring the land subsidence area in a coastal urban area with InSAR and GNSS. *Sensors* **2019**, *19*, 3181. [CrossRef]
33. Zebker, H.; Villasenor, J. Decorrelation in interferometric radar echoes. *IEEE Trans. Geosci. Remote Sens.* **1992**, *30*, 950–959. [CrossRef]
34. Mallick, J.; AlMesfer, M.K.; Singh, V.P.; Falqi, I.I.; Singh, C.K.; Alsubih, M.; Ben Kahla, N. Evaluating the NDVI–rainfall relationship in Bisha watershed, Saudi Arabia using non-stationary modeling technique. *Atmosphere* **2021**, *12*, 593. [CrossRef]
35. Yuan, X.; Li, L.; Chen, X.; Shi, H. Effects of precipitation intensity and temperature on NDVI-based grass change over Northern China during the period from 1982 to 2011. *Remote Sens.* **2015**, *7*, 10164–10183. [CrossRef]
36. Nasirzadehdizaji, R.; Cakir, Z.; Sanli, F.B.; Abdikan, S.; Pepe, A.; Calò, F. Sentinel-1 interferometric coherence and backscattering analysis for crop monitoring. *Comput. Electron. Agric.* **2021**, *185*, 106118. [CrossRef]

37. Villarroya-Carpio, A.; Lopez-Sanchez, J.M.; Engdahl, M.E. Sentinel-1 interferometric coherence as a vegetation index for agriculture. *Remote Sens. Environ.* **2022**, *280*, 113208. [CrossRef]
38. Osmanoğlu, B.; Sunar, F.; Wdowinski, S.; Cabral-Cano, E. Time series analysis of InSAR data: Methods and trends. *ISPRS J. Photogramm. Remote Sens.* **2016**, *115*, 90–102. [CrossRef]
39. Treuhaft, R.N.; Siqueira, P.R. Vertical structure of vegetated land surfaces from interferometric and polarimetric radar. *Radio Sci.* **2000**, *35*, 141–177. [CrossRef]
40. Smith, G.; Dammert, P.B.G.; Askne, J. Decorrelation mechanisms in C-band SAR interferometry over boreal forest. In *Microwave Sensing and Synthetic Aperture Radar*; SPIE: Bellingham, WA, USA, 1996; Volume 2958, p. 300.
41. Lazecký, M.; Spaans, K.; González, P.J.; Maghsoudi, Y.; Morishita, Y.; Albino, F.; Elliott, J.; Greenall, N.; Hatton, E.; Hooper, A.; et al. LiCSAR: An automatic InSAR tool for measuring and monitoring tectonic and volcanic activity. *Remote Sens.* **2020**, *12*, 2430. [CrossRef]
42. Zwieback, S.; Hensley, S.; Hajnsek, I. Assessment of soil moisture effects on L-band radar interferometry. *Remote Sens. Environ.* **2015**, *164*, 77–89. [CrossRef]
43. Nolan, M.; Fatland, D.R. Penetration depth as a DInSAR observable and proxy for soil moisture. *IEEE Trans. Geosci. Remote Sens.* **2003**, *41*, 532–537. [CrossRef]
44. Kornelsen, K.C.; Coulibaly, P. Advances in soil moisture retrieval from synthetic aperture radar and hydrological applications. *J. Hydrol.* **2013**, *476*, 460–489. [CrossRef]
45. Ullmann, T.; Sauerbrey, J.; Hoffmeister, D.; May, S.M.; Baumhauer, R.; Bubenzer, O. Assessing spatiotemporal variations of sentinel-1 InSAR coherence at different time scales over the atacama desert (Chile) between 2015 and 2018. *Remote Sens.* **2019**, *11*, 2960. [CrossRef]

Disclaimer/Publisher's Note: The statements, opinions and data contained in all publications are solely those of the individual author(s) and contributor(s) and not of MDPI and/or the editor(s). MDPI and/or the editor(s) disclaim responsibility for any injury to people or property resulting from any ideas, methods, instructions or products referred to in the content.